Robust DNS-driven turbulence modeling for hypersonic flows

P. Calvi*, P. Cinnella*, X. Gloerfelt**, J. Breil***,****, M. Olazabal***
Corresponding author: paul.calvi@sorbonne-universite.fr
* Institut Jean Le Rond d'Alembert, Sorbonne Université, CNRS, France.
** Laboratoire DynFluid, Arts et Métiers Institute of Technology, France.
*** CEA CESTA, France.
**** I2M, INP Bordeaux, France.

Abstract: Data-driven corrections to RANS turbulence closures are typically learned as discrepancies between a baseline model and high-fidelity data. Ensuring a numerically robust and consistent baseline is therefore essential to avoid compensating discretization errors rather than genuine model deficiencies. To this end, the present work relies on the high-order, low-dissipation finite-difference solver MUSICAA, also used to generate the reference DNS databases. A logarithmic reformulation of the k–ω SST model ($\hat{\omega} = \log \omega$) is implemented to mitigate the singular near-wall behavior of the specific dissipation rate and is verified over a range of flat-plate turbulent boundary layers from $M = 2$ to 9.22, together with several dilatational-dissipation and density-gradient compressibility corrections. Consistent with the literature, these corrections tend to degrade predictions of skin friction, heat transfer, and separation. A data-driven correction based on the SpaRTA methodology, trained on a hypersonic compression-ramp configuration, is then assessed on two shock-wave/turbulent-boundary-layer interaction cases at $M = 7.2$ and shown to substantially improve predictive accuracy.

Keywords: Hypersonics, Computational Fluid Dynamics, Numerical methods, Turbulence Modeling, Data-Driven.

1. Introduction

Shock-wave/turbulent-boundary-layer interactions (STBLI) are among the most challenging flow phenomena encountered in hypersonic aerodynamics. They arise in a wide range of applications, including engine inlets, control surfaces, and compression-ramp configurations, and are characterized by strong pressure gradients, shock-induced separation, and intense aerodynamic heating [1, 2]. Accurate prediction of wall pressure, skin friction, and heat transfer remains essential for the design of thermal protection systems and propulsion components. Despite the rapid progress of high-fidelity simulation techniques, Reynolds-Averaged Navier–Stokes (RANS) methods remain the primary engineering tool for the analysis of realistic hypersonic configurations. However, turbulence models commonly employed in RANS simulations continue to exhibit significant deficiencies in high-Mach-number flows. Most models of practical relevance were developed and calibrated using incompressible or weakly compressible canonical flows, and their predictive capability often deteriorates when confronted with strong compressibility effects, wall cooling, or shock-induced separation. Numerous compressibility corrections have therefore been proposed over the last decades, including modifications accounting for dilatational dissipation [3, 4, 5] and density-gradient effects in turbulent transport [6, 7]. Nevertheless, recent assessments indicate that substantial discrepancies remain for quantities of primary engineering interest, particularly wall heat transfer and shock-interaction characteristics [8].

Among two-equation closures, the k–ω Shear Stress Transport (SST) model [9] remains one of the most widely used turbulence models for aerodynamic applications. Although generally regarded as a robust baseline model, its performance in hypersonic turbulent boundary layers and STBLI remains mixed. In particular, both validation studies [10] and recent *a priori* analyses based on DNS databases [11] have identified significant deficiencies in several modeled terms, even when conventional compressibility corrections are included. At the same time, turbulence modeling is increasingly evolving toward data-driven methodologies. Symbolic-regression and machine-learning approaches are now routinely formulated as corrections to existing RANS closures rather than as entirely new models [12, 13]. In practice, the SST model is frequently adopted as the baseline upon which these corrections are learned. Consequently, the numerical robustness and consistency of the baseline formulation become critical issues. Indeed, a learned correction may compensate not only deficiencies of the physical model but also numerical errors arising from the discretization or implementation of the underlying closure. Ensuring a stable and numerically well-behaved baseline model is therefore a prerequisite for reliable data-driven turbulence modeling.

A specific numerical difficulty of k–ω-type closures stems from the near-wall behavior of the specific dissipation rate. For smooth walls, the asymptotic solution behaves as $\omega \sim \frac{\nu}{y^2}$ as $y \longrightarrow 0$, which formally implies an unbounded wall value. In practical computations this singularity is replaced by a large finite wall value depending on the first-cell distance, as in the usual Menter prescription [9]. Although effective in many finite-volume solvers, this treatment introduces grid-dependent boundary conditions and extremely steep near-wall gradients. These features may become problematic on highly resolved meshes and when combined with low-dissipation or high-order discretizations. The issue is particularly acute in hypersonic cooled-wall boundary layers, where the first-cell height is typically very small.

Several strategies have been proposed to alleviate the numerical difficulties associated with the singular near-wall behaviour of the specific dissipation rate. A first class of approaches preserves the original asymptotic solution while introducing a change of variables. Among them, logarithmic formulations, originally proposed by Bassi *et al.* [14] for discontinuous Galerkin discretizations and subsequently adopted in several high-order solvers, replace the transport equation for ω by an equation for $\hat{\omega} = \log \omega$. Although this transformation does not remove the wall singularity, since $\hat{\omega} \sim -2 \log y$ as $y \longrightarrow 0$, it substantially compresses the dynamic range of the solution and reduces the stiffness associated with the y^{-2} growth of ω. Furthermore, the inverse transformation, $\omega = \exp(\hat{\omega})$ ensures positivity of the specific dissipation rate by construction, preventing non-physical negative values that may otherwise compromise the evaluation of eddy viscosity and cross-diffusion terms.

More recently, alternative reformulations have been proposed with the explicit objective of eliminating the singular wall value. Chedevergne [15] introduced an SST formulation in which the transported variable vanishes at the wall while the physical ω field is recovered through the addition of an analytical near-wall contribution. Durbin and Yin [16] proposed a closely related $k - \omega_0$ formulation based on a regularized dissipation variable that also satisfies a homogeneous wall boundary condition. These approaches yield transported variables with bounded wall values and may improve numerical discretization in the near-wall region. However, they modify the mathematical structure of the original model through source terms proportional to $1/y^2$ in the k equation and do not guarantee positivity.

When learning data-driven corrections, control of numerical errors is also of paramount importance to avoid compensating discretization artifacts through the learned terms. To minimize consistency errors between the databases used for model development and the turbulence model implementation itself, the present work relies on the high-order finite-difference solver MUSICAA [17], which is also employed to generate the reference databases based on direct numerical simulation (DNS). Owing to its intrinsically low numerical dissipation and nodal finite-difference discretization, MUSICAA requires a particularly robust formulation of the SST model. In the present work, we therefore focus on logarithmic formulations.

This work constitutes a first step toward improving the robustness and accuracy of SST-based turbulence modeling for hypersonic flows. First, the baseline transport equations of the k–ω SST model and their logarithmic reformulation are reviewed. Next, the logarithmic formulation is assessed over a range of Mach numbers and wall-temperature conditions and compared against reference solutions. Dilatation-dissipation corrections are incorporated into the proposed framework and systematically assessed for hypersonic turbulent boundary layers. Finally, they are validated against high-fidelity simulations of hypersonic shock-wave/turbulent-boundary-layer interactions, and compared to preliminary results for data-driven corrections based on the Sparse regression of Reynolds stress anisotropy (SpaRTA) algorithm [18], extended to compressible flow configurations.

2. Governing equations and numerical methods

2.1 Standard k–ω SST model

The standard k–ω SST model, introduced by Menter in 1994 [9], is a two-equation model for the turbulent kinetic energy k, and the specific dissipation rate $\omega = \epsilon/\beta^* k$, where ϵ denotes the turbulent dissipation rate. The two transport equations written in conservation form are

$$\frac{\partial \rho k}{\partial t} + \frac{\partial \rho u_j k}{\partial x_j} = \mathcal{P} - \beta^* \rho k \omega + \frac{\partial}{\partial x_j}\left[(\mu + \sigma_k \mu_t)\frac{\partial k}{\partial x_j}\right] \tag{1}$$

$$\frac{\partial \rho \omega}{\partial t} + \frac{\partial \rho u_j \omega}{\partial x_j} = \frac{\rho \alpha}{\mu_t}\mathcal{P} - \beta \rho \omega^2 + \frac{\partial}{\partial x_j}\left[(\mu + \sigma_\omega \mu_t)\frac{\partial \omega}{\partial x_j}\right] + (1 - F_1) CD_{k\omega}\,, \tag{2}$$

where the cross-diffusion source term is

$$CD_{k\omega} = 2\rho \frac{\sigma_{\omega_2}}{\omega}\frac{\partial k}{\partial x_j}\frac{\partial \omega}{\partial x_j}. \tag{3}$$

The turbulent eddy viscosity μ_t is given by

$$\mu_t = \frac{a_1 \rho k}{\max\{a_1 \omega, F_2 \Omega\}}\,, \tag{4}$$

where a_1=0.31 is the Bradshaw constant for shear layers, Ω is the vorticity magnitude

$$\Omega = \sqrt{2 W_{ij} W_{ij}} \quad \text{with} \quad W_{ij} = \frac{1}{2}\left(\frac{\partial u_i}{\partial x_j} - \frac{\partial u_j}{\partial x_i}\right)\,. \tag{5}$$

The two blending functions F_1 and F_2 are defined as

$$F_1 = \tanh(\arg_1^4) \quad \text{with} \quad \arg_1 = \min\{\max\{\xi_1, \xi_2\}, \xi_3\} \tag{6}$$

$$F_2 = \tanh(\arg_2^2) \quad \text{with} \quad \arg_2 = \max\{2\xi_1, \xi_2\}\,, \tag{7}$$

where

$$\xi_1 = \frac{\sqrt{k}}{\beta^* \omega d_w} \quad , \quad \xi_2 = \frac{500\nu}{\omega d_w^2} \quad , \quad \xi_3 = \frac{4\sigma_{\omega 2}\rho k}{\max\left\{CD_{k\omega}, 10^{-20}\right\} d_w^2}, \tag{8}$$

d_w being the distance to the nearest wall. The turbulent kinetic energy production term, $\mathcal{P}$ in (1), is reformulated as a function of the anisotropic strain-rate tensor components $S^\dagger_{ij}$

$$\mathcal{P} = \tau_{ij}\frac{\partial u_i}{\partial x_j} = 2\mu_t S^\dagger_{ij} S^\dagger_{ji} - \frac{2}{3}\rho k \frac{\partial u_k}{\partial x_k} \quad \text{with} \quad S^\dagger_{ij} = S_{ij} - \frac{1}{3}\frac{\partial u_k}{\partial x_k}\delta_{ij}\,. \tag{9}$$

Besides, the production term is limited, replacing $\mathcal{P}$ by

$$\min\{\mathcal{P}, 20\beta^* \rho \omega k\}\,. \tag{10}$$

Finally, the two sets of constants are blended using F_1:

$$\sigma_k = F_1\sigma_{k_1} + (1-F_1)\sigma_{k_2} \quad \text{with} \quad \sigma_{k_1}=0.85\ ,\ \sigma_{k_2}=1.0 \tag{11}$$

$$\sigma_\omega = F_1\sigma_{\omega_1} + (1-F_1)\sigma_{\omega_2} \quad \text{with} \quad \sigma_{\omega_1}=0.5\ ,\ \sigma_{\omega_2}=0.856 \tag{12}$$

$$\beta = F_1\beta_1 + (1-F_1)\beta_2 \quad \text{with} \quad \beta_1=0.075\ ,\ \beta_2=0.0828 \tag{13}$$

$$\alpha = F_1\alpha_1 + (1-F_1)\alpha_2 \quad \text{with} \quad \alpha_1 = \frac{\beta_1}{\beta^*} - \frac{\sigma_{\omega 1}\kappa^2}{\sqrt{\beta^*}}\ ,\ \alpha_2 = \frac{\beta_2}{\beta^*} - \frac{\sigma_{\omega 2}\kappa^2}{\sqrt{\beta^*}} \tag{14}$$

given β^*=0.09 and the von Kármán constant κ=0.41.

2.2 Logarithmic formulation of ω equation

A first difficulty encountered when applying k–ω models in high-order solvers arises from the steep spatial variations of the turbulence variables at the boundary-layer edge, as well as within mixing layers and wakes. These sharp gradients may generate numerical oscillations, even in incompressible-flow simulations. Locally, such oscillations can lead to very small values of ω, resulting in excessively large eddy viscosities (Eq.(4)) and ultimately compromising the stability of the solver.

A second limitation concerns the wall boundary condition imposed on the specific dissipation rate. While k vanishes at the wall, ω theoretically tends to infinity. In practice, Menter [9] recommends prescribing a finite wall value for ω that depends on the distance to the first grid point, Δy_{wall}, according to

$$\omega_{\text{wall}} = \frac{60\nu_{\text{wall}}}{\beta^*\Delta y_{\text{wall}}^2}. \tag{15}$$

For finely resolved meshes, this prescribed value can become extremely large, leading to steep near-wall gradients of ω. These gradients may in turn trigger spurious numerical oscillations, particularly when high-order centered discretization schemes are employed. In hypersonic flows with cooled walls, this issue can be even more severe because the near-wall grid spacing is typically very small ($\Delta y^+_{\text{wall}} \leq 0.5$).

To address this issue, which has also been reported in high-order discontinuous Galerkin methods, Bassi *et al.* [14] proposed a variable transformation for the Wilcox k–ω model [19]. This formulation has been used in DLR codes for both Wilcox and SST k–ω models[20]. The approach consists of solving the transport equation for the logarithm of the specific dissipation rate, $\hat{\omega} = \log(\omega)$. Applying this transformation to the k–ω SST model yields

$$\frac{\rho k}{\partial t} + \frac{\partial \rho u_j k}{\partial x_j} - \frac{\partial}{\partial x_j}\left[(\mu + \sigma_k\mu_t)\frac{\partial k}{\partial x_j}\right] = \mathcal{P} - \beta^*\rho k \mathrm{e}^{\hat{\omega}} \tag{16}$$

$$\frac{\rho\hat{\omega}}{\partial t} + \underbrace{\frac{\partial \rho u_j \hat{\omega}}{\partial x_j}}_{\text{advection}} \underbrace{- \frac{\partial}{\partial x_j}\left[(\mu + \sigma_\omega\mu_t)\frac{\partial \hat{\omega}}{\partial x_j}\right]}_{\text{diffusion}} = \underbrace{\frac{\rho\alpha \mathrm{e}^{-\hat{\omega}}}{\mu_t}\mathcal{P}}_{\text{production}} - \underbrace{\beta\rho\mathrm{e}^{\hat{\omega}}}_{\text{destruction}} + \underbrace{(1-F_1)CD_{k\omega}\mathrm{e}^{-\hat{\omega}}}_{\text{cross-diff.}} + \underbrace{(\mu + \sigma_\omega\mu_t)\frac{\partial \hat{\omega}}{\partial x_j}\frac{\partial \hat{\omega}}{\partial x_j}}_{\text{add. source}}. \tag{17}$$

The transformation introduces an additional source term proportional to the square of the gradient of $\hat{\omega}$. Its primary advantage is to reduce the dynamic range of ω, especially within the viscous sublayer where its gradients are largest. As a result, the wall boundary treatment becomes more robust, mitigating the shortcomings of the original formulation. Furthermore, the transformation guarantees the positivity of ω by construction, which is particularly advantageous when ω appears in the denominator, for example in

$$\mu_t = \frac{a_1\rho k}{\max\{a_1\exp(\hat{\omega}),\ F_2\Omega\}} \quad \text{with} \quad \exp(\hat{\omega}) > 0. \tag{18}$$

2.3 Compressibility corrections

A first class of compressibility corrections seeks to account for dilatational dissipation effects. Following the analysis of Gatski [21], the turbulent dissipation rate can be decomposed into a solenoidal component, ϵ_s, which is represented in conventional turbulence closures, and a dilatational component, ϵ_d, associated with compressibility effects. Most existing models express the latter as a function of ϵ_s and the turbulent Mach number $M_t = \sqrt{2k}/a$ according to

$$\epsilon_d = \xi^* F(M_t)\, \epsilon_s,$$

where the function $F(M_t)$ depends on the specific model:

$$\text{Sarkar [3]}: \quad F(M_t) = M_t^2, \tag{19}$$

$$\text{Zeman [4]}: \quad F(M_t) = \left\{1 - \exp\left[-\left(\frac{M_t - M_{t0}}{\Lambda}\right)^2\right]\right\} \mathcal{H}(M_t - M_{t0}), \tag{20}$$

$$\text{Wilcox [5]}: \quad F(M_t) = \left[M_t^2 - M_{t0}^2\right] \mathcal{H}(M_t - M_{t0}). \tag{21}$$

The model parameters, including the threshold turbulent Mach number M_{t0} and, in the case of Zeman's formulation, the parameter Λ, vary among the different references. In the framework of the k–ω model, these corrections modify the destruction terms through

$$\beta_c^* = \beta^* \left[1 + \xi^* F(M_t)\right] \quad , \quad \beta_c = \beta - \beta^* \xi^* F(M_t). \tag{22}$$

A second class of compressibility corrections aims to account for density variations in the turbulent diffusion terms. Among the most widely used formulations are those proposed by Catris and Aupoix [6] and subsequently extended by Otero *et al.* [7]. These approaches derive modified transport equations that preserve the asymptotic consistency of turbulence models in strongly compressible flows.

2.4 Data-driven framework based on sparse symbolic regression

The Sparse Regression of Turbulent stress Anisotropy (SpaRTA) method is a data-driven modeling framework based on symbolic regression that seeks to derive physically interpretable corrections to the Reynolds-stress anisotropy tensor used in RANS closures. Inspired by Explicit Algebraic Reynolds Stress Models (EARSM) [22], SpaRTA was originally developed for incompressible flows, where it demonstrated significant improvements in the prediction of separated-flow configurations [18, 23].

The central idea is to identify the discrepancy between the Reynolds-stress anisotropy predicted by a turbulence model and that obtained from high-fidelity data, and to use this discrepancy as the target quantity for model improvement. However, the turbulent scales predicted by RANS closures generally differ from those observed in high-fidelity simulations [24]. Furthermore, any modification of the Reynolds-stress closure should remain consistent with the auxiliary transport equations, such as those governing k and ω in the SST model. To address these issues, Schmelzer *et al.* [18] introduced the k-corrective frozen-RANS methodology. The objective is to determine a modified specific dissipation rate, denoted ω_{frozen}, that preserves the RANS turbulence time scale while reproducing the statistical state of the high-fidelity data. This quantity is obtained by solving the ω transport equation with the mean-flow field frozen to the high-fidelity solution. The resulting field is then used to evaluate the dimensionless anisotropy discrepancy tensor, b_{ij}^{Δ}.

To account for the influence of the correction on the turbulence model and to represent additional unresolved physical mechanisms, such as compressibility effects, the residual of the frozen-k equation is evaluated at each iteration. This residual defines a second target quantity, denoted R, which appears as an additional source term in the frozen-ω equation. Since this contribution is generally interpreted as an additional production mechanism, it is commonly represented through an equivalent dimensionless stress tensor, b^R_{ij}.

Both tensors are subsequently approximated using the Generalized Eddy Viscosity Model (GEVM) proposed by Pope [25]. In this formulation, the classical Boussinesq hypothesis is extended by introducing nonlinear contributions expressed as a polynomial expansion over a tensor basis. The expansion coefficients are functions of a set of invariant quantities, while the tensor basis itself is constructed from the symmetric and skew-symmetric parts of the dimensionless strain-rate and rotation-rate tensors.

SpaRTA then formulates the closure-identification problem by constructing a library of nonlinear candidate functions. This procedure transforms the nonlinear modeling problem into a linear regression problem that can be addressed using sparse-inference techniques. The original implementation relied on a deterministic strategy combining elastic-net regression with a subsequent ridge-regression refinement step. More recently, Cherroud [23] proposed a Sparse Bayesian Learning (SBL) formulation. In contrast to deterministic approaches, SBL provides probability distributions for the inferred coefficients, whose mean values correspond to maximum-likelihood estimates. This probabilistic framework is particularly attractive for uncertainty quantification and the assessment of model-form uncertainty.

2.5 Numerical methods

The standard k–ω (§ 2.1) and logarithmic k–$\hat{\omega}$ (§ 2.2) formulations have been implemented in the in-house CFD solver MUSICAA [17]. MUSICAA solves the compressible Navier–Stokes equations in strong conservation form on multi-block curvilinear structured meshes using high-order finite-difference discretizations formulated in transformed coordinates. The metric terms satisfy the geometric conservation requirements and preserve a uniform freestream solution to machine precision.

For the present RANS computations, both the mean-flow and turbulence-model transport equations are discretized using fourth-order centered finite differences. Convective and viscous fluxes are evaluated with standard fourth-order finite-difference operators, providing a consistent spatial accuracy throughout the computational domain. The turbulence equations are solved in conservative form and employ the same discretization framework as the mean-flow equations.

Numerical stability is ensured through a fourth-order adaptive filtering procedure applied to both the flow and turbulence variables. In smooth regions, the filter selectively removes unresolved grid-to-grid oscillations while preserving the formal order of accuracy of the underlying scheme. In the vicinity of shock waves and other strong gradients, a Jameson-type sensor activates a nonlinear low-order dissipation mechanism, providing the robustness required for shock capturing while minimizing excessive numerical damping away from discontinuities.

The Navier–Stokes and turbulence-model equations are solved in an uncoupled manner. At each pseudo-time iteration, the mean-flow equations are first advanced using the current turbulent viscosity field, after which the turbulence transport equations are updated using the newly computed flow solution. Time integration is performed with a classical four-stage explicit Runge–Kutta scheme combined with local time stepping to accelerate convergence toward steady state. Depending on the flow conditions and grid resolution, the Courant–Friedrichs–Lewy (CFL) number is progressively increased during the computation and typically remains in the range $0.05 \leq \text{CFL} \leq 0.5$.

For the SSTlog formulation, the transport equation is solved for the logarithm of the specific dissipation rate, $\hat{\omega} = \log(\omega)$. All source, diffusion, and cross-diffusion terms are evaluated consistently with the transformed variable. In contrast to the standard SST formulation, the positivity of ω is guaranteed by construction, eliminating the need for ad hoc clipping procedures that may otherwise affect robustness and convergence.

3. Assesment of k–$\hat{\omega}$ SST formulation and compressibility corrections

3.1 High Mach number flat plate validation cases

The NASA validation case for 2D zero-pressure-gradient (ZPG) turbulent flat-plate boundary layers at high Mach numbers [26] is used to assess the k–$\hat{\omega}$ SST formulation (hereafter referred to as SSTlog). The grids provided by NASA for the flat plate verification case (levels 0 to 3) are slightly adapted by suppressing the inlet zone (for which a symmetry condition was employed), yielding a series of nested grids with 450×384, 232×192, 100×100 and 50×50 points. Inlet conditions are prescribed at x=0, imposing a freestream turbulence intensity of Tu_∞=0.002% and a freestream turbulent viscosity $\mu_{t,\infty}/\mu_\infty$=0.009. For supersonic Mach numbers, the inflow boundary condition set all variables and these variables are extrapolated from the interior domain at the outflow boundary. A non-reflecting characteristic boundary condition is used at the top boundary and an isothermal wall condition is enforced along the bottom boundary. The plate has a non-dimensional length of 2 with a Reynolds number per unit length Re=15 million. The freestream temperature is T_∞=540.6°R and the four computed cases are given in Table 1.

Case	M_∞	T_w/T_∞	T_w/T_{aw}
M2T1	2	1.712	1.0
M5T1	5	1.090	1.0
M5T05	5	2.725	0.5
M5T02	5	5.450	0.2

Table 1: Supersonic flat-plate validation cases.

Cases M2T1 and M5T1 corresponds to pseudo-adiabatic conditions, whereas M5T05 and M5T02 are cold-wall configurations representative of hypersonic flows with ratio of wall to ideal adiabatic temperatures between 0.2 and 0.5, where the ideal adiabatic temperature is defined as

$$T_{aw} = T_\infty \left(1 + \frac{\gamma - 1}{2} M_\infty^2\right) .$$

3.1.1 Grid convergence study for SSTlog

First, a grid-convergence study was performed to evaluate the sensitivity of the SSTlog model to mesh resolution. Figure 1 presents the streamwise velocity profiles in wall units together with the empirical van Driest-transformed correlation [27] and results obtained with the NASA code CFL3D [26] on the finest grid level. It should be noted that CFL3D solves the conservative form of the k–ω SST model in an uncoupled manner using a simplified production term (denoted SST-Vm on the NASA Turbulence Modeling Resource website), in which the square of vorticity magnitude Ω^2 replaces $2S^\dagger_{ij}S^\dagger_{ji}$ in Eq. (9) and the spherical contribution $-\frac{2}{3}\rho k \frac{\partial u_k}{\partial x_k}$ is neglected. At Mach 2, excellent agreement is observed with both the van Driest correlation and CFL3D on all grid levels, indicating a weak sensitivity to mesh resolution. The Mach 5 cases, however, exhibit a more pronounced grid dependence. In addition, the van Driest transformation is only approximate for strongly cooled-wall conditions, as illustrated by the case $T_w/T_{aw} = 0.2$. The skin-friction coefficient is defined as

$$C_f = \frac{\tau_w}{\frac{1}{2}\rho_\infty u_\infty^2}, \tag{23}$$

and its streamwise evolution is reported in Fig. 3 for the four cases.

For case M2T1, C_f is essentially grid-converged throughout the region of interest, $4000 < Re_\theta < 13,000$, where Re_θ denotes the Reynolds number based on momentum thickness. Grid-resolution effects are confined to the numerical transition region near the inlet. For reference, the DNS-based correlation of

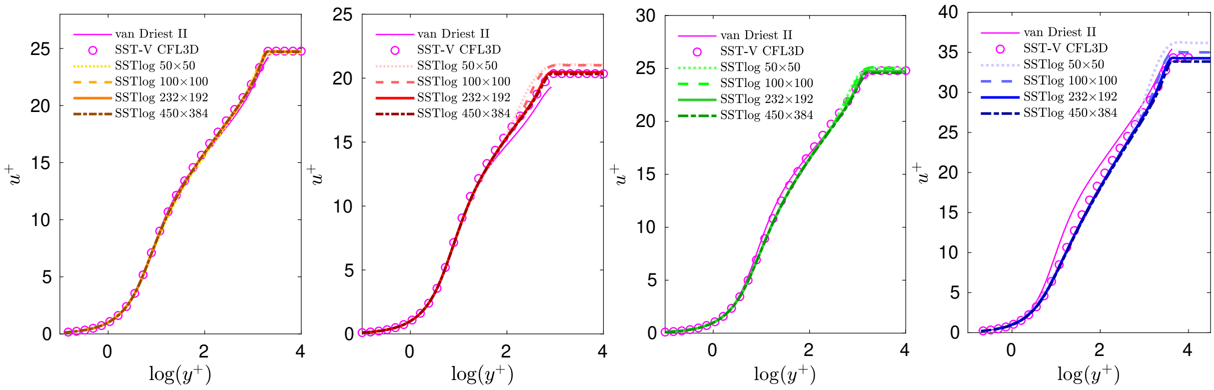

(a) Case M2T1 (b) Case M5T1 (c) Case M5T05 (d) Case M5T02

Figure 1: Grid convergence study for the velocity profiles at Re_θ=10 000.

Ceci *et al.* [28], $C_f = A_3 Re_\theta^{-B_3}$ (A_3=0.0174; B_3=0.245), derived from the high-resolution DNS of Wenzel *et al.* [29] and Ceci *et al.* [28] up to $Re_\theta \approx 6000$, is also shown. The RANS predictions remain remarkably close to this DNS reference.

The mesh sensitivity becomes more significant at Mach 5, particularly for cases M5T1 and M5T02. Because all Mach 5 simulations are performed at the same Reynolds number and plate length, variations in wall temperature lead to different grid resolutions when expressed in wall units (Table 2). The stronger sensitivity observed for M5T1 can therefore be attributed to its comparatively coarse near-wall resolution. Case M5T02 is especially demanding because the intense wall cooling generates a very thin thermal boundary layer that requires enhanced spatial resolution. As shown in Fig. 3(d), the two finest grids do not yet provide complete convergence, and the SSTlog predictions remain slightly above those obtained with CFL3D. Nevertheless, further mesh refinement is expected to recover close agreement, as demonstrated in § 3.2.1 for a Mach 5 turbulent boundary layer at $Re = 5 \times 10^6$ and strong wall cooling, where a near-wall resolution of $\Delta y_w^+ = 0.15$ and $\Delta x^+ \approx 1720$ is achieved on the grid level 1 at the same index.

The observed mesh dependence is further illustrated by the eddy-viscosity profiles shown in Fig. 2. Interestingly, the eddy viscosity remains noticeably grid-dependent even for the Mach 2 cases, despite the fact that the primary quantities of interest, such as the velocity profiles and skin-friction coefficient, are already converged.

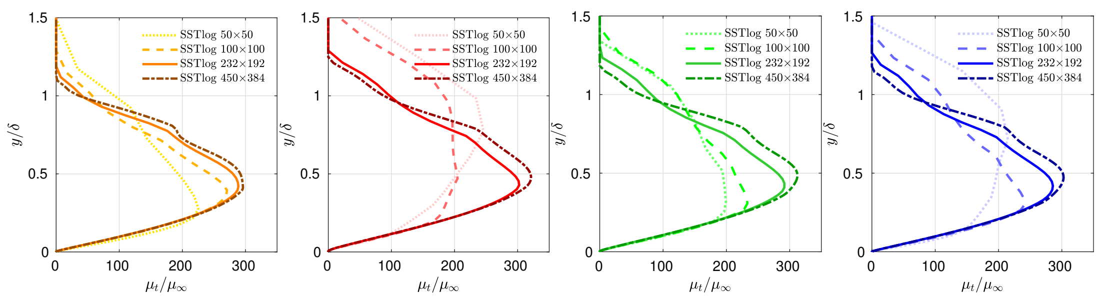

(a) Case M2T1 (b) Case M5T1 (c) Case M5T05 (d) Case M5T02

Figure 2: Grid convergence study: eddy viscosity profiles at Re_θ=10 000.

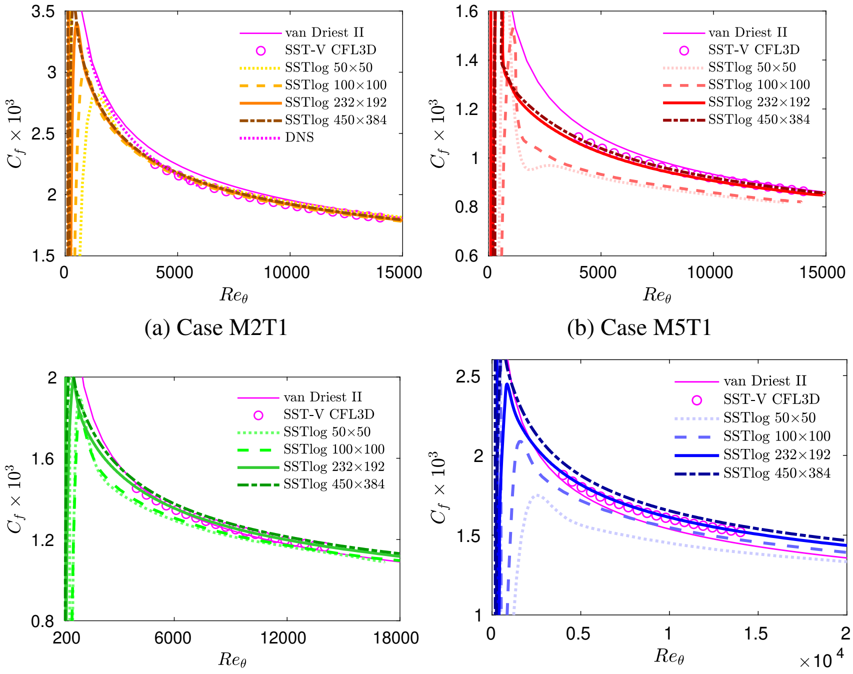

(a) Case M2T1 (b) Case M5T1

(c) Case M5T05 (d) Case M5T02

Figure 3: Grid convergence study for the skin-friction coefficient.

Case	Grid3 (50×50)		Grid2 (100×100)		Grid1 (232×192)		Grid0 (450×384)	
	Δy_w^+	Δx^+	Δy_w^+	Δx^+	Δy_w^+	Δx^+	Δy_w^+	Δx^+
M2T1	2.4	26789	1.2	13095	0.6	5564	0.3	2897
M5T1	2.8	69882	1.4	34485	0.7	15245	0.35	7896
M5T05	2.4	48008	1.2	25054	0.6	10478	0.3	5379
M5T02	1.6	18214	0.8	10839	0.4	4914	0.2	2578

Table 2: Grid resolution measured at reference location where Re_θ=10 000.

3.1.2 Comparison of SST and SSTlog formulations

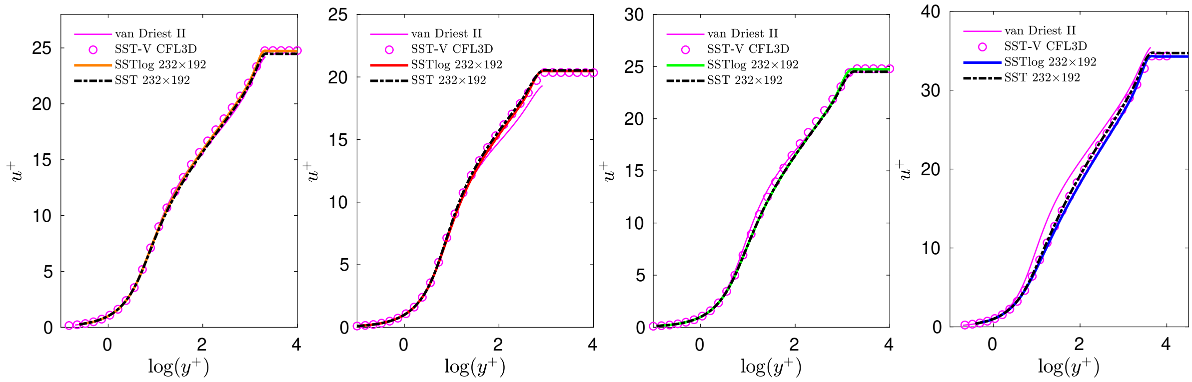

(a) Case M2T1 (b) Case M5T1 (c) Case M5T05 (d) Case M5T02

Figure 4: Comparison of SSTlog and SST formulations: velocity profiles at Re_θ=10 000.

The results for the quantities of interest, namely the velocity profiles and skin-friction coefficients, are presented in Figs. 4 and 5 for the four cases on grid level 1 (232×192). Both formulations produce very similar velocity profiles, with only minor differences in the wake region. These discrepancies can be attributed to the slightly different skin-friction levels predicted by the two formulations, as shown in Fig. 5.

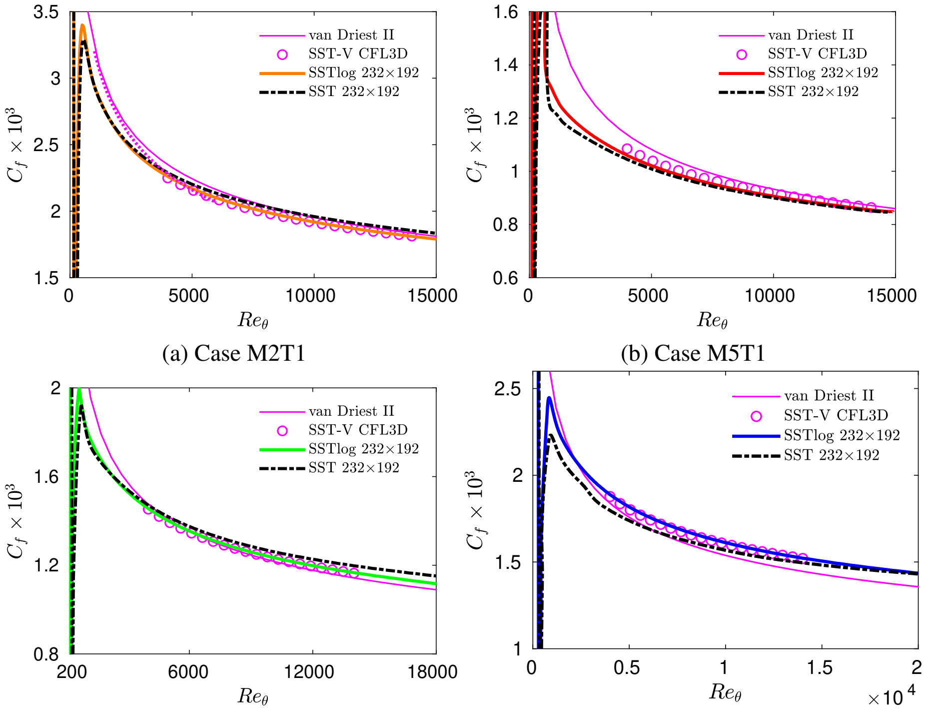

(a) Case M2T1 (b) Case M5T1

(c) Case M5T05 (d) Case M5T02

Figure 5: Comparison of SSTlog and SST formulations: skin-friction coefficient evolutions.

To investigate these differences further, logarithmic profiles of the eddy viscosity and specific dissipation rate are reported in Figs. 6 and 7. The most notable feature is the presence of numerical oscillations in the near-wall distributions of the turbulence quantities. These oscillations are particularly pronounced for cases M5T1 and M5T02, which were previously identified as the most sensitive to grid resolution. The origin of these oscillations can be traced to the very large values of ω prescribed at the wall (theoretically unbounded), which generate extremely steep gradients in the near-wall region. As a consequence, spurious oscillations may develop, leading locally to negative values of ω and, in severe cases, to solver divergence.

A detailed examination of the flow field indicates that the inlet region, where the leading-edge shock is formed, is especially susceptible to such numerical instabilities. To prevent solver failure, the baseline SST implementation requires the introduction of a lower bound on ω. In the present work, ω is constrained to remain above either its freestream value or a fraction thereof to account for the streamwise decay of the turbulence level. Specifically, the simulations employ the limiter:

$$\omega \leftarrow \max\left\{\omega, 0.1\omega_\infty\right\}.$$

Although this safeguard enables successful computations with the standard SST formulation, it may adversely affect the convergence properties of the solver. This behaviour is illustrated in Fig. 8. At Mach 2, both formulations exhibit comparable convergence histories, whereas at Mach 5 the residuals associated with the turbulence equations stagnate for the standard SST model. In contrast, the SSTlog formulation achieves a significantly lower residual level, demonstrating its improved numerical robustness. Moreover,

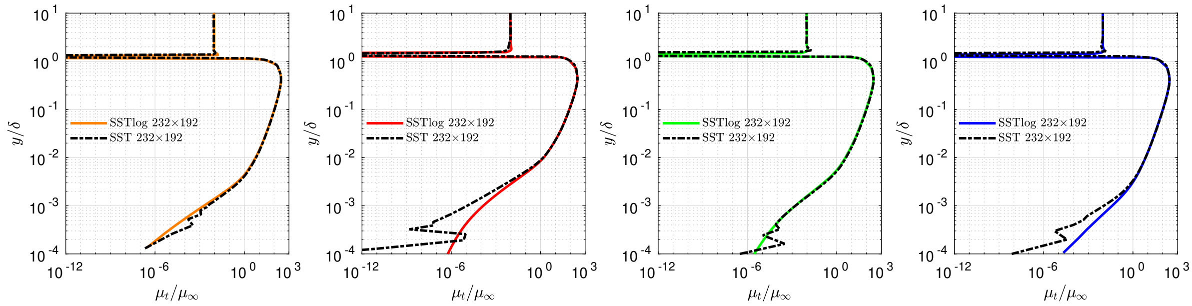

(a) Case M2T1 (b) Case M5T1 (c) Case M5T05 (d) Case M5T02

Figure 6: Comparison of SSTlog and SST formulations: eddy viscosity profiles at Re_θ=10 000.

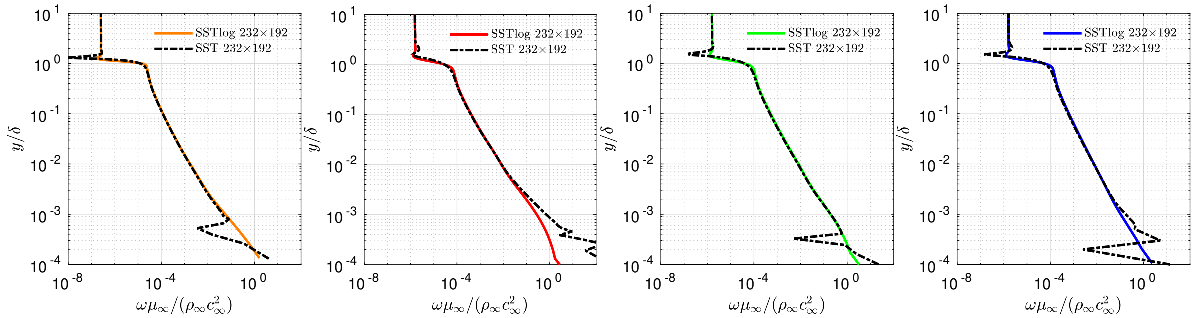

(a) Case M2T1 (b) Case M5T1 (c) Case M5T05 (d) Case M5T02

Figure 7: Comparison of SSTlog and SST formulations: specific dissipation profiles at Re_θ=10 000.

the introduction of such a limiter modifies the original model equations and may affect the predicted turbulence levels in regions where the clipping becomes active.

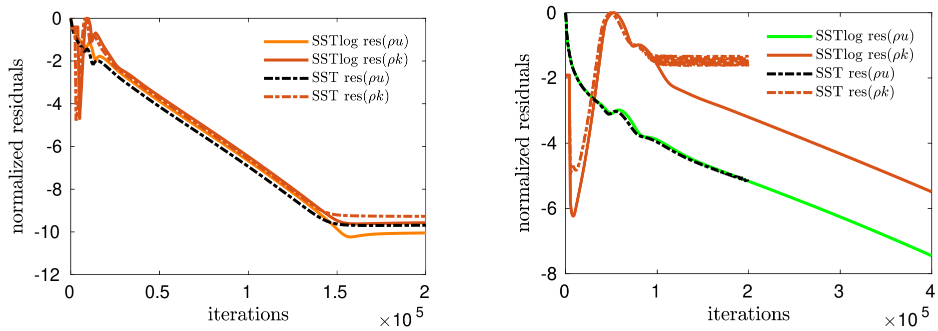

(a) Case M2T1 (b) Case M5T1

Figure 8: Comparison of SSTlog and SST formulations: evolutions of residuals (L_2-norm of solution increments averaged over all grid points).

3.2 Compressibility corrections for hypersonic boundary-layer flows (HTBL)

3.2.1 Highly-cooled M=5 HTBL

We first assess the impact of compressibility corrections on a hypersonic flat-plate turbulent boundary layer. by comparing our results with those reported by Rumsey [30] for a Mach 5 flow with $T_w/T_\infty = 1$, corresponding to $T_w/T_{aw} = 0.167$. The same NASA flat-plate grid level is employed (232×192) with a unit Reynolds number of 5×10^6. The plate length is kept equal to $L = 2$, yielding $Re_L = 10^7$. Compared with the cases presented in § 3.1, this configuration provides a finer near-wall resolution. The same numerical setup and boundary conditions are adopted, with the inlet located at the plate leading edge. The three compressibility corrections described in § 2.3, which account for dilatational dissipation effects, are investigated: the corrections proposed by Zeman (20), Wilcox (21), and Sarkar (19). The first two were also examined by Rumsey [30], and the same model parameters are employed here. For Zeman's correction, $\xi^* = 0.75$, $M_{t0} = 0.2$, and $\Lambda = 0.66$ are used, whereas Wilcox's correction is applied with $\xi^* = 2$ and $M_{t0} = 0.25$.

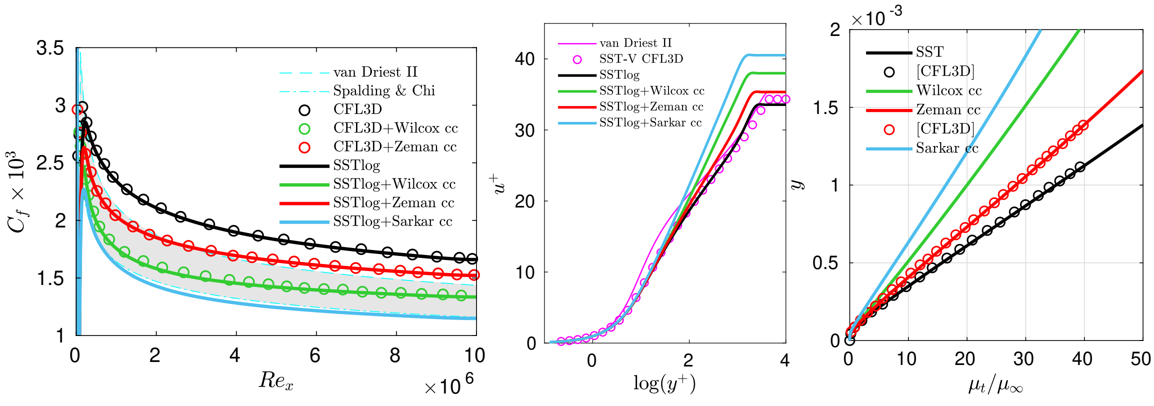

Figure 9: Effects of compressibility corrections on highly-cooled HTBL: (a) skin friction evolution (the gray-shaded area is the region between the van Driest and Spalding & Chi correlations); (b) velocity profiles at Re_x=5×10^6 and (c) near-wall distribution of μ_t/μ_∞ at Re_x=5×10^6.

The results are presented in Fig. 9. Figure 9(a) shows the skin-friction coefficient as a function of Re_x, together with the correlations of van Driest [27] and Spalding & Chi [31]. The region bounded by these two correlations is shaded in gray and may be regarded as a plausible range of reference values. First, the SSTlog predictions obtained without compressibility correction and with either the Zeman or Wilcox correction closely reproduce the CFL3D results reported by Rumsey [30], thereby validating the present implementation. Second, all compressibility corrections reduce the predicted skin-friction coefficient relative to the baseline SST model. The Wilcox correction produces a significant reduction, placing the results well within the gray band. Zeman's correction yields values closer to the upper bound defined by the van Driest correlation, whereas Sarkar's correction leads to skin-friction levels approaching the lower bound given by the Spalding–Chi correlation. The corresponding velocity profiles at the midpoint of the plate ($Re_x = 5 \times 10^6$) are displayed in Fig. 9(b). Since no reference solution is available for this configuration, the velocity profile of case M5T02 is also shown for comparison. Although the wall temperature is less severe in that case, it provides a useful indication of the expected trend. To elucidate the reduction in skin friction induced by the dilatational-dissipation corrections, a close-up view of the non-dimensional eddy viscosity is presented in Fig. 9(c). All three corrections reduce the eddy viscosity in the near-wall region relative to the uncorrected SST model. The magnitude of this reduction closely follows the observed decrease in skin-friction levels, indicating that the corrections primarily act through a weakening of the turbulent momentum transport in the inner part of the boundary layer.

3.2.2 Imperial College Gun Tunnel HTBL at M=9.22

We now consider a more realistic configuration for which experimental heat-transfer data are available. The test case corresponds to the experiments of Elfstrom and Coleman conducted in the Imperial College

Gun Tunnel [32, 33]. Elfstrom measured velocity profiles using Pitot probes, while Coleman reported wall heat-flux distributions along the plate. The freestream flow consists of nitrogen at Mach 9.22 with a unit Reynolds number of 4.7×10^7 m^{-1}, a freestream pressure $p_\infty = 2700$ Pa, and a freestream temperature $T_\infty = 64.5$ K. The wall temperature is maintained at $T_w = 295$ K, yielding a ratio $T_w/T_r = 0.3$, where the recovery temperature is defined as

$$T_r = T_\infty \left(1 + r\frac{\gamma - 1}{2} M_\infty^2\right), \qquad r = 0.89.$$

This hypersonic turbulent boundary layer corresponds to the incoming flow upstream of compression ramps with various deflection angles, recently investigated by our group [34]. The DNS data used in the present study correspond to the flat-plate region upstream of the ramp and were obtained using the same numerical framework as the current study, except that tenth-order finite-difference schemes and filtering are employed for the discretization of the inviscid fluxes. The computational mesh comprises $1950 \times 320 \times 640$ grid points, corresponding to resolutions in wall units of approximately $\Delta x^+ \approx 6.6$, $\Delta y_w^+ \approx 0.3$, and $\Delta z^+ \approx 3.3$. The SSTlog simulations, with and without the dilatational-dissipation corrections introduced in the previous section, are performed on the NASA level-1 grid (232×192), dimensionalized to match the experimental plate length of 60 cm. Velocity profiles at the second measurement station of Elfstrom, located at $x = 15.6$ in (≈ 40 cm), are compared with the experimental data and DNS results in Fig. 10.

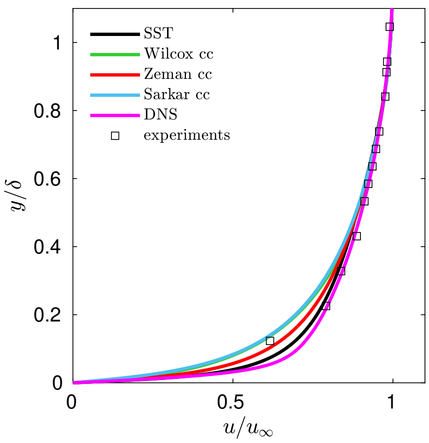

(a)

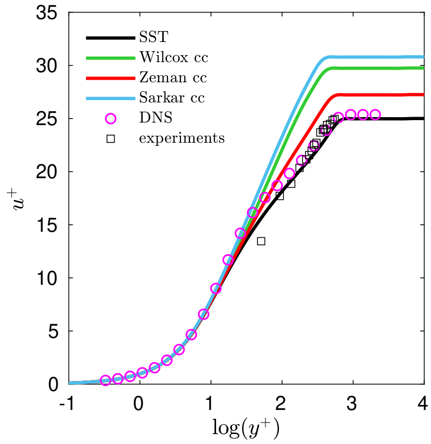

(b)

Figure 10: Effects of compressibility corrections: velocity profiles at x=15.6 in for HTBL at M=9.22, T_w/T_r=0.3, compared with DNS [34] and experiments [32].

Figure 10(a) shows the streamwise velocity normalized by its edge value as a function of the wall-normal coordinate normalized by the boundary-layer thickness δ. The DNS profile is noticeably fuller than the RANS predictions. Among the latter, the baseline SSTlog model provides the closest agreement with DNS, followed by SSTlog with Zeman's correction, while the Wilcox and Sarkar corrections yield nearly identical profiles and the largest departure from the DNS result. It should also be noted that the experimental point closest to the wall is generally considered unreliable due to measurement uncertainties. The comparison in wall units, reported in Fig. 10(b), further confirms that the SSTlog model without compressibility correction provides the best agreement with both DNS and experimental data. The upward shift of the logarithmic region observed when dilatational-dissipation corrections are activated reflects a reduction in friction velocity. This trend is consistent with the skin-friction distributions shown in Fig. 11(a), where the baseline SSTlog model remains in satisfactory agreement with the DNS over the range $6500 \leq Re_\theta \leq 8500$. The wall heat transfer is expressed in terms of the Stanton number,

$$C_h = \frac{q_w}{\rho_\infty c_p u_\infty (T_r - T_w)}, \qquad q_w = -\kappa \left.\frac{\partial T}{\partial y}\right|_w, \tag{24}$$

where c_p denotes the specific heat at constant pressure and κ the thermal conductivity.

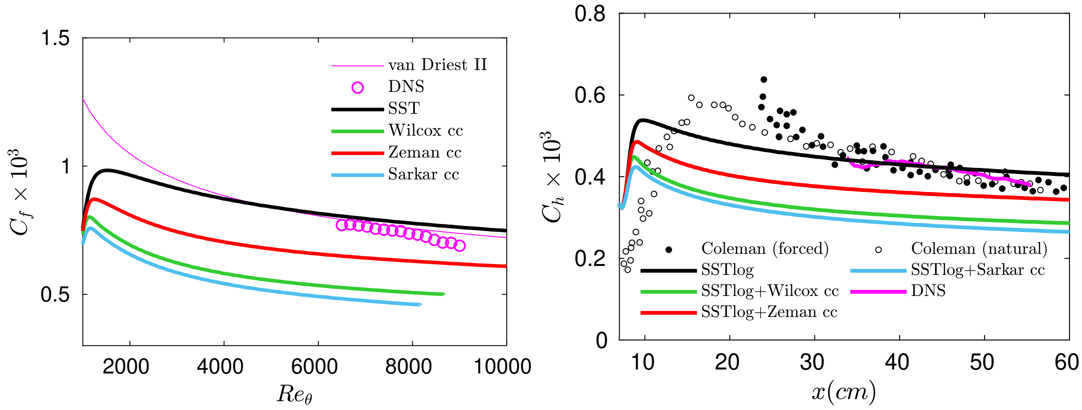

(a) (b)

Figure 11: Effects of compressibility corrections: (a) skin friction and (b) wall heat flux for HTBL at M=9.22, T_w/T_r=0.3, compared with DNS [34] and experiments [33].

The corresponding results are presented in Fig. 11(b) together with Coleman's measurements. Two sets of experimental data are available, corresponding respectively to natural transition and to a tripped boundary layer designed to promote an earlier onset of turbulence. The baseline SSTlog model predicts Stanton numbers in reasonable agreement with both the experimental measurements and the DNS data. In contrast, the inclusion of dilatational-dissipation corrections systematically reduces the wall heat flux and leads to a significant underprediction of the Stanton number. For the present cooled-wall hypersonic boundary layer, these corrections therefore appear to degrade the agreement with the available reference data rather than improve it.

4. Application to compression ramps and comparison with augmented models

4.1 Presentation STBLI configurations and reference database

In this section, the proposed k–$\hat{\omega}$ SST formulation is assessed on two hypersonic shock-wave/turbulent-boundary-layer interaction (STBLI) configurations. The logarithmic formulation is employed to ensure robust and stable computations, while several compressibility corrections from the literature are incorporated to evaluate their performance in the presence of strong shock-induced pressure gradients. Both configurations correspond to experiments conducted by Schreyer *et al.* [35] in the Princeton Mach 8 hypersonic wind tunnel. The operating conditions are characterized by a total pressure and temperature of $p_0 = 1365.6$ kPa and $T_0 = 760$ K, respectively, an edge Mach number of $M_e = 7.2$, and a wall temperature of $T_w = 340$ K.

The first configuration consists of an 8° compression ramp. Under these conditions, the shock generated by the geometric deflection remains attached and the incoming turbulent boundary layer does not separate. The second configuration employs the same freestream conditions and inflow turbulent boundary layer but with a larger ramp angle of 33°. The resulting adverse pressure gradient is sufficiently strong to induce shock-induced boundary-layer separation, leading to the formation of a large recirculation bubble. Downstream of the interaction region, the compression ramp is followed by an expansion section to limit tunnel blockage effects. For both cases, the reference length scale is chosen as the incoming boundary-

Config.	Grid sizes	Δy_w^+
SC8	210×150	0.3
SC33	370×150	0.3

Table 4: Compression corner RANS simulations mesh grid properties.

layer thickness, $\delta_{\mathrm{ref},SC} = 9.8$ mm, estimated experimentally at a location $x = -0.64, \delta_{\mathrm{ref},SC}$ upstream of the corner.

In support of ongoing developments of data-driven turbulence closures, these experiments were recently reproduced by direct numerical simulation using the MUSICAA solver [34]. The resulting databases were generated with the objective of training and assessing sparse-regression turbulence models based on the SpaRTA methodology [18], summarized in § 2.4. The numerical framework is described in § 2.5. Compared with the present RANS computations, the DNS employs tenth-order centered finite-difference discretizations for the inviscid fluxes, while shock capturing is achieved through a combination of the Jameson sensor and the modified Ducros sensor proposed by Hendrickson *et al.* [36]. The turbulent inflow boundary layer is synthetically generated using the Random Fourier Modes (RFM) technique coupled with a Cholesky decomposition to reproduce the target Reynolds-stress anisotropy [37]. The main parameters of the experimental, DNS, and RANS configurations are summarized in Table 3.

Code	M_e	α	T_e [K]	T_w [K]	p_e [kPa]	$Re_{\theta,\mathrm{in}}$	Grid sizes
SC8	7.2	8°	63.5	430.0	1.38	7000	$2500 \times 300 \times 320$
SC33	7.2	33°	63.5	430.0	1.38	7000	$2250 \times 320 \times 640$

Table 3: Database setting of summary.

4.2 Assessment on SST-correction for SBLI configurations

For the RANS computations, the inflow turbulent boundary layer is obtained from an auxiliary zero-pressure-gradient (ZPG) flat-plate simulation performed under the same freestream conditions as the reference experiment. The inflow station is selected such that the boundary-layer properties at the compression corner closely match those of the reference DNS. The mesh characteristics employed for the two compression-ramp configurations are summarized in Table 4.

In addition to the baseline k–$\hat{\omega}$ SST formulation, the compressibility corrections considered in the present study include the dilatational-dissipation models of Sarkar and Zeman, as well as the density-corrected diffusion formulation proposed by Catris & Aupoix. These corrections are implemented within the logarithmic SST framework and assessed against the available DNS and experimental data.

The resulting predictions are also compared with a data-driven correction obtained using the SpaRTA methodology. The correction was trained on the SC8 database and subsequently propagated in both the SC8 and SC33 configurations. It should be kept in mind that the application of the correction to the SC8 configuration corresponds to an in-sample bias, as it is evaluated on the same data used for training. This limitation should be considered when interpreting the results. Moreover, although the model captures several important trends, systematic discrepancies are observed even for the training configuration, indicating that the inferred correction should not be regarded as an exact representation of the target closure. The resulting model, denoted M_{SC8}, takes the form

$$M_{SC8}: \begin{cases} b_{ij}^{\Delta} & = (5.81 + 1.63 M_t) \left(S_{il}^* \Omega_{lj}^* - \Omega_{il}^* S_{lj}^* \right), \\ b_{ij}^{R} & = 0.86 S_{ij}^*, \end{cases} \tag{25}$$

where S^*_{ij} and Ω^*_{ij} denote the dimensionless strain-rate and rotation-rate tensors defined by

$$S^*_{ij} = \frac{S^\dagger_{ij}}{||\mathbf{S}^\dagger||_2 + \omega}, \quad \Omega^*_{ij} = \frac{\Omega_{ij}}{||\mathbf{\Omega}||_2 + \omega}. \tag{26}$$

In the following, the compression corner is located at $x' = 0$ for both configurations, where x' denotes the curvilinear streamwise coordinate. All wall quantities of interest (QoIs) are non-dimensionalized using the edge-flow properties evaluated at $x' = -15, \delta_{\mathrm{ref},SC}$ upstream of the interaction. The RANS results indicate that the compressibility corrections considered in the present study, particularly the dilatational-dissipation models, generally deteriorate the agreement with the reference data. Their primary effect is a reduction of the turbulent eddy viscosity, which in turn lowers the predicted skin-friction coefficient. For the SC33 configuration (Fig. 13), the resulting underprediction of wall shear stress significantly increases the extent of the separated-flow region. The recirculation-bubble length is approximately doubled when Zeman's correction is applied and becomes even larger with Sarkar's correction. A similar trend is observed for the wall heat transfer. By reducing turbulent transport in the near-wall region, the compressibility corrections decrease the wall-normal temperature gradient and consequently lead to an underprediction of the Stanton number C_h.

Such detrimental effects have previously been reported by Sciacovelli *et al.* [11], who performed an *a priori* assessment of the k–ω SST model using several DNS databases of hypersonic turbulent boundary layers. Their analysis examined the influence of various compressibility corrections on the turbulent kinetic-energy budget and highlighted the limitations of dilatational-dissipation-based formulations in hypersonic regimes. More specifically, Wilcox [5] identified such corrections as potentially detrimental for the prediction of shock-wave/turbulent-boundary-layer interactions.

In contrast, the SpaRTA-based correction M_{SC8} significantly improves the agreement with the reference database. For the SC8 configuration (Fig. 12), the augmented model not only increases the wall-shear-stress level toward the reference values but also provides a more accurate representation of the interaction region in the vicinity of the compression corner. These improvements demonstrate the ability of data-driven corrections to recover missing physical mechanisms that are not adequately represented by the baseline turbulence model.

Nevertheless, the present results also illustrate a well-known limitation of data-driven turbulence modeling. While the learned correction improves the prediction in the targeted interaction region, it may simultaneously degrade portions of the flow that are already reasonably well captured by the baseline RANS model, such as the incoming equilibrium turbulent boundary layer. This issue has motivated recent developments aimed at localizing data-driven corrections. For example, Oulghelou *et al.* [38] proposed learning specialized corrections for different canonical flow configurations and subsequently blending them using a Random Forest regressor trained to identify regions where a given correction is expected to be beneficial.

Although M_{SC8} substantially improves the prediction of wall shear stress, it appears to do so at the expense of a slight deterioration in the wall-pressure distribution for SC8 configuration. As shown in Fig. 12, the pressure rise along the compression ramp tends to be slightly overpredicted relative to the reference data. To quantify these discrepancies, the relative root-mean-square error (RRMSE) is evaluated for several QoIs and for each model m, according to

$$\mathrm{RRMSE}_m = \sqrt{\frac{\sum_{i=1}^{N}\left(QoI^{(m)}(x_i) - QoI^{(DNS)}(x_i)\right)^2}{\sum_{i=1}^{N}\left(QoI^{(SST)}(x_i) - QoI^{(DNS)}(x_i)\right)^2}}. \tag{27}$$

Figures 14 and 15 summarize the relative root-mean-square errors for the different quantities of interest. Overall, these results indicate a clear improvement for most QoIs in both configurations when using the data-driven model, compared with the baseline SST model, while also highlighting a deterioration

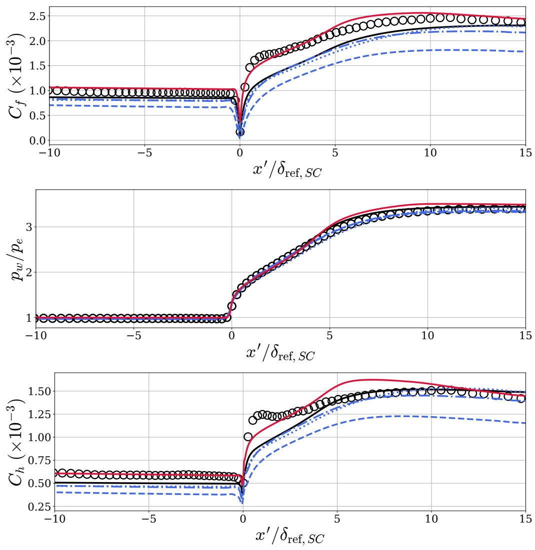

Figure 12: Wall quantities of interest for SC8 configuration. Comparison between SST (—), Sarkar (– –), Zeman (–·), Catris & Aupoix (···) compressible correction and model M_{SC8} (—).

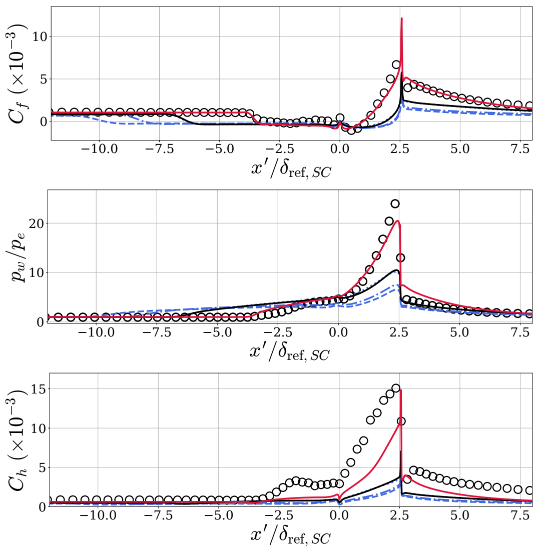

Figure 13: Wall quantities of interest for SC33 configuration. Comparison between SST (—), Sarkar (– –), Zeman (–·), Catris & Aupoix (···) compressible correction and model M_{SC8} (—).

of the results obtained using compressibility corrections. It is worth noting that the use of Zeman's or Sarkar's compressibility corrections improves the wall-pressure prediction in Fig. 14. This result should be interpreted with caution, as the wall pressure in the SC8 configuration is already accurately predicted by the baseline model, which leads to a degeneration of the relative error metric (27). This figure nevertheless highlights a slight deterioration in the wall-pressure prediction obtained with M_{SC8}. However, this loss of accuracy remains limited when compared with the substantial improvements observed for skin friction and wall heat transfer, for which the errors are reduced by approximately 40 to 60%.

More importantly, the model exhibits encouraging generalization capabilities when applied to the SC33 configuration, which involves a significantly stronger adverse pressure gradient and a large separation bubble, while preserving the same freestream conditions as the training case. As shown in Fig. 13, the correction substantially improves the prediction of the separation and reattachment locations, leading to a much more accurate estimate of the recirculation-bubble length. The resulting skin-friction distribution is also in markedly better agreement with the reference data. These improvements can be attributed, at least in part, to the additional source term R appearing in Eq. (25). Since b_{ij}^{R} is proportional to the dimensionless strain-rate tensor, the corresponding correction acts as an additional production mechanism in the turbulent kinetic-energy budget. The net effect is an increase in turbulent stresses, which strengthens the coupling between the turbulence field and the mean flow. In separated-flow regions, this enhanced turbulent transport promotes momentum exchange across the shear layer and contributes to a reduction of the separation extent.

Unlike the SC8 case, the correction also improves the wall-pressure prediction in the SC33 configuration. This improvement is primarily associated with the more accurate prediction of the recirculation-bubble size, which directly influences the pressure distribution throughout the interaction region. In addition, the pressure peak generated near the downstream ledge is captured more accurately than with the baseline model.

The heat-transfer predictions are likewise improved by the M_{SC8} correction in both configurations, with reductions of the RRMSE approaching 40%. For the SC8 case, this improvement appears to be obtained at the expense of a slight deterioration of the skin-friction prediction in the incoming turbulent boundary layer (Fig. 12). Within the interaction region itself, the heat-transfer distribution remains imperfectly reproduced, despite the overall increase in heat-transfer levels. Nevertheless, the corrected model recovers the reference trend downstream of the interaction and provides a significantly improved prediction in the redevelopment region beyond $x' = 10, \delta_{\mathrm{ref},SC}$.

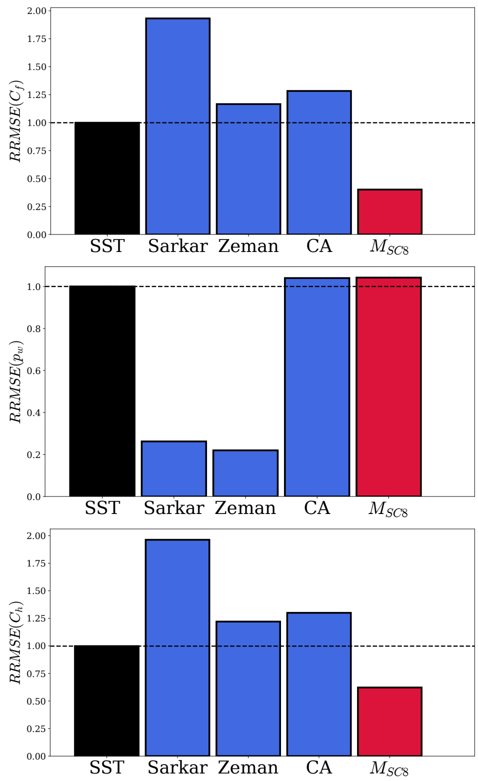

Figure 14: Relative error bar for wall quantities of interest prediction in SC8 configuration for every models.

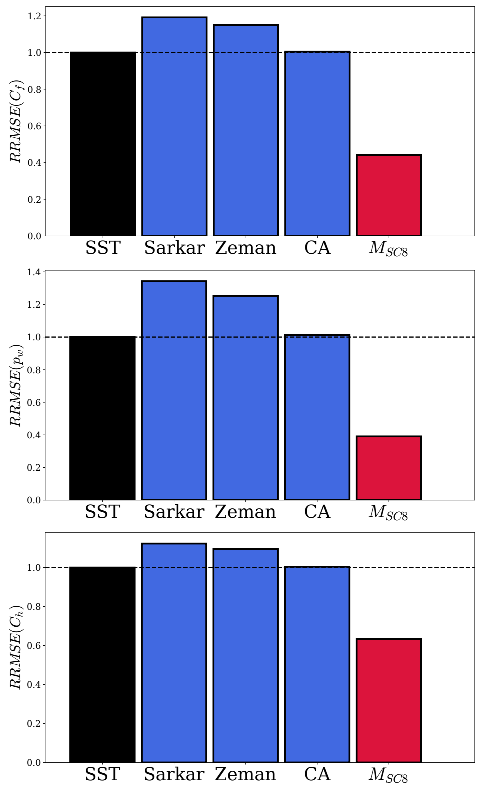

Figure 15: Relative error bar for wall quantities of interest prediction in SC33 configuration for every models.

5. Conclusions and outlook

In this work, the logarithmic formulation of the specific-dissipation-rate transport equation has been implemented in the high-order finite-difference solver MUSICAA and assessed over a range of hypersonic turbulent boundary-layer configurations covering different Mach numbers and wall-temperature conditions. The proposed formulation was found to provide predictions comparable to those of the standard SST model for the quantities of engineering interest, while substantially improving numerical robustness. In particular, the logarithmic transformation alleviates difficulties associated with the singular near-wall behavior of the specific dissipation rate and eliminates the need for ad hoc clipping procedures to preserve positivity. These properties make the formulation especially attractive for low-dissipation, high-order discretizations, for which the standard SST model may exhibit stability and convergence issues.

The framework was further extended by incorporating several compressibility corrections available in the literature. Their performance was evaluated on hypersonic shock-wave/turbulent-boundary-layer interaction configurations for which high-fidelity DNS databases are available. Consistent with previous *a priori* and *a posteriori* studies, the corrections considered in the present work generally failed to improve the predictive capability of the baseline SST model and, in several cases, degraded the agreement with reference data for skin friction, wall heat transfer, and separation characteristics.

A key outcome of this work is the successful integration of a robust SST formulation within the same numerical framework used to generate the DNS databases. This consistency minimizes discrepancies arising from numerical discretization and provides a particularly suitable environment for the development of data-driven turbulence closures. As a first step in this direction, a SpaRTA-based correction trained on a hypersonic compression-corner database was implemented and evaluated. Despite its simplicity, the resulting augmented model yielded substantial improvements in the prediction of shock-wave/turbulent-boundary-layer interactions, including encouraging results for a separated-flow configuration not included in the training set.

Future work will focus on the construction of more general data-driven closures using larger hypersonic DNS databases and on the development of localization and blending strategies capable of restricting learned corrections to regions where they are beneficial. Combined with the robust logarithmic SST formulation proposed herein, such approaches offer a promising pathway toward improved turbulence modeling for hypersonic applications.

References

[1] J.D. Anderson. *Hypersonic and High-temperature Gas Dynamics*. AIAA education series. American Institute of Aeronautics and Astronautics, 2006.

[2] H. Babinsky and J. Harvey. *Shock Wave-Boundary-Layer Interactions*. Cambridge University Press, New York, 2011.

[3] S. Sarkar, G. Erlebacher, M.Y. Hussaini, and H.O. Kreiss. The analysis and modelling of dilatational terms in compressible turbulence. *J. Fluid Mech.*, 227:473–493, 1991.

[4] O. Zeman. Dilatation dissipation: The concept and application in modeling compressible mixing layers. *Phys. Fluids*, 2(2):178–188, 1990.

[5] D.C. Wilcox. Dilatation-dissipation corrections for advanced turbulence models. *AIAA Journal*, 30(11):2639–2646, 1992.

[6] S. Catris and B. Aupoix. Density corrections for turbulence models. *Aerospace Science and Technology*, 4(1):1–11, 2000.

[7] G.J. Otero R., A. Patel, R. Diez, and R. Pecnik. Turbulence modelling for flows with strong variations in thermo-physical properties. *International Journal of Heat and Mass Transfer*, 73:114–123, 2018.

[8] P. Raje, E. Parish, J.-P. Hickey, P. Cinnella, and K. Duraisamy. Recent developments and research needs in turbulence modeling of hypersonic flows. *Phys. Fluids*, 37:031304, 2025.

[9] F.R. Menter. Two-equation eddy-viscosity turbulence models for engineering applications. *AIAA Journal*, 32(8):1598–1605, 1994.

[10] C.J. Roy and F.G. Blottner. Review and assessment of turbulence models for hypersonic flows. *Progress in Aerospace Sciences*, 42:469–530, 2006.

[11] L. Sciacovelli, A. Cannici, D. Passiatore, and P. Cinnella. A priori tests of turbulence models for compressible flows. *International Journal of Numerical Methods for Heat & Fluid Flow*, 34:2808–2831, 2024.

[12] P. Cinnella. Data-driven turbulence modeling. In M.A. Mendez and A. Parente, editors, *Machine Learning for Fluid Dynamics*, VKI Lecture Series. Von Karman Institute for Fluid Dynamics, Rhode-St-Genèse, Belgium, 2025.

[13] P. Cinnella. Symbolic regression methods. In K. Duraisamy, editor, *Data Driven Analysis and Modeling of Turbulent Flows*, Computation and Analysis of Turbulent Flows, chapter 9, pages 355–396. Academic Press, 2025.

[14] F. Bassi, A. Crivellini, S. Rebay, and M. Savini. Discontinuous Galerkin solution of the Reynolds-averaged Navier–Stokes and k–ω turbulence model equations. *Computers and Fluids*, 34(4):507–540, 2005.

[15] F. Chedevergne. The k–ω shear stress transport model with ω=0 at the wall. *AIAA Journal*, 63(11):5021–5024, 2025.

[16] P. Durbin and Z. Yin. Reformulation of the ω equation of the k–ω model. *AIAA Journal*, 64(5):2679–2682, 2026.

[17] A. Bienner, X. Gloerfelt, Ö. Yal¸cin, and P. Cinnella. Multiblock parallel high-order implicit

residual smoothing time scheme for compressible Navier-Stokes equations. *Computers and Fluids*, 269:106138, 2024.

[18] M. Schmelzer, R.P. Dwight, and P. Cinnella. Discovery of algebraic Reynolds-stress models using sparse symbolic regression. *Flow, Turbulence and Combustion*, 104(2-3):579–603, 2019.

[19] D.C. Wilcox. *Turbulence Modeling for CFD*. DCW Industries, Inc., La Canada CA, 3rd edition, 2006.

[20] M. Müller and C. Morsbach. A logarithmic ω-equation formulation for turbulence models in harmonic balance solvers. In *6th European Conference on Computational Mechanics (ECCM6), 7th European Conference on Computational Fluid Dynamics (ECFD7)*, volume 1631, pages 1–12, Glasgow, UK, June 11-15 2018.

[21] T.B. Gatski. Modeling compressibility effects on turbulence. In J.H. Ferziger O. Métais, editor, *New Tools in Turbulence Modelling, Les Houches School, May 21–31, 1996*, volume 5 of *Centre de Physique des Houches*, Berlin, Heidelberg, 1997. Springer.

[22] T.B. Gatski and C.G. Speziale. On explicit algebraic stress models for complex turbulent flows. *J. Fluid Mech.*, 254:59–78, 1993.

[23] S. Cherroud, X. Merle, P. Cinnella, and X. Gloerfelt. Sparse Bayesian learning of explicit algebraic Reynolds-stress models for turbulent separated flows. *International Journal of Heat and Mass Transfer*, 98:109047, 2023.

[24] H. Mandler and B. Weigand. On frozen-RANS approaches in data-driven turbulence modeling: Practical relevance of turbulent scale consistency during closure inference and application. *International Journal of Heat and Mass Transfer*, 97:109017, 2022.

[25] S.B. Pope. A more general effective-viscosity hypothesis. *J. Fluid Mech.*, 72:331–340, 1975.

[26] NASA, Turbulence Modeling Resource page, https://tmbwg.github.io/turbmodels/, 2026.

[27] F.M. White. *Viscous fluid flow*. McGraw-Hill, 1974.

[28] A. Ceci, A. Palumbo, J. Larsson, and S. Pirozzoli. Numerical tripping of high-speed turbulent boundary layers. *Theoret. Comput. Fluid Dynamics*, 36:865–886, 2022.

[29] C. Wenzel, P. Vogler, J.M.F. Peter, M.J. Kloker, and U. Rist. Application of a JPEG 2000-based data compression algorithm to DNS of compressible turbulent boundary layers up to Re_θ=6600. In Resch M.M. Nagel W.E., Kröner D.H., editor, *High Performance Computing in Science and Engineering '20*, pages 295–313. Springer, Cham, 2021.

[30] C.L. Rumsey. Compressibility considerations for k-ω turbulence models in hypersonic boundary-layer applications. *Journal of Spacecraft and Rockets*, 47(1):11–20, 2010. also NASA/TM-2009-215705.

[31] D.B. Spalding and S.W. Chi. The drag of a compressible turbulent boundary layer on a smooth flat plate with and without heat transfer. *J. Fluid Mech.*, 18(1):117–143, 19.

[32] G.M. Elfstrom. *Turbulent separation in hypersonic flow*. PhD thesis, Department of Aeronautics, Imperial College, London, 1971.

[33] G.T. Coleman, C. Osborne, and J.L. Stollery. Heat transfer from a hypersonic turbulent boundary layer on a flat plate. *J. Fluid Mech.*, 60(2):257–271, 1973.

[34] X. Gloerfelt, P. Calvi, P. Cinnella, J. Breil, and M. Olazabal. High-fidelity simulations of hypersonic shock wave/turbulent boundary layer interaction over compression ramps. In *Workshop Direct and Large-Eddy Simulation (DLES15)*, Delft, the Netherlands, May 20-22 2026.

[35] A.-M. Schreyer, D. Sahoo, O.J.H. Williams, and A.J. Smits. Experimental investigation of two hypersonic shock/turbulent boundary-layer interactions. *AIAA Journal*, 56(12):4830–4844, 2018.

[36] T.R. Hendrickson, A. Kartha, and G.V. Candler. An improved Ducros sensor for the simulation of compressible flows with shocks. *Fluid Dynamics Conference,* 25-29 June, Atlanta, GA, AIAA Paper 2018-3710, 2018.

[37] H. Guo, P. Jiang, L. Ye, and Y. Zhu. An efficient and low-divergence method for generating inhomogeneous and anisotropic turbulence with arbitrary spectra. *J. Fluid Mech.*, 970:A2, 2023.

[38] M. Oulghelou, S. Cherroud, X. Merle, and P. Cinnella. Machine-learning-assisted blending of data-driven turbulence models, 2025. https://arxiv.org/abs/2410.14431.